Supplementary Materials for

Thermodynamic Optimization of Atomically Thin Iron-Based Compounds for Mid-Infrared Laser Power Scaling

This file includes:

Supplementary Figs. 1 to 14

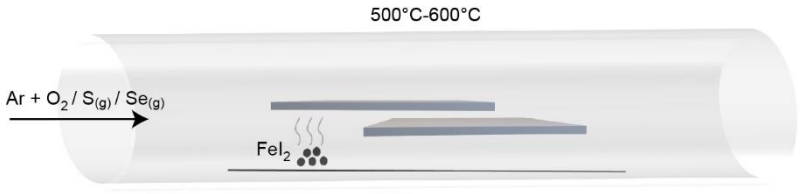

Supplementary Fig. 1 | Schematic illustration of the synthesis process for 2D Fe-based crystals.

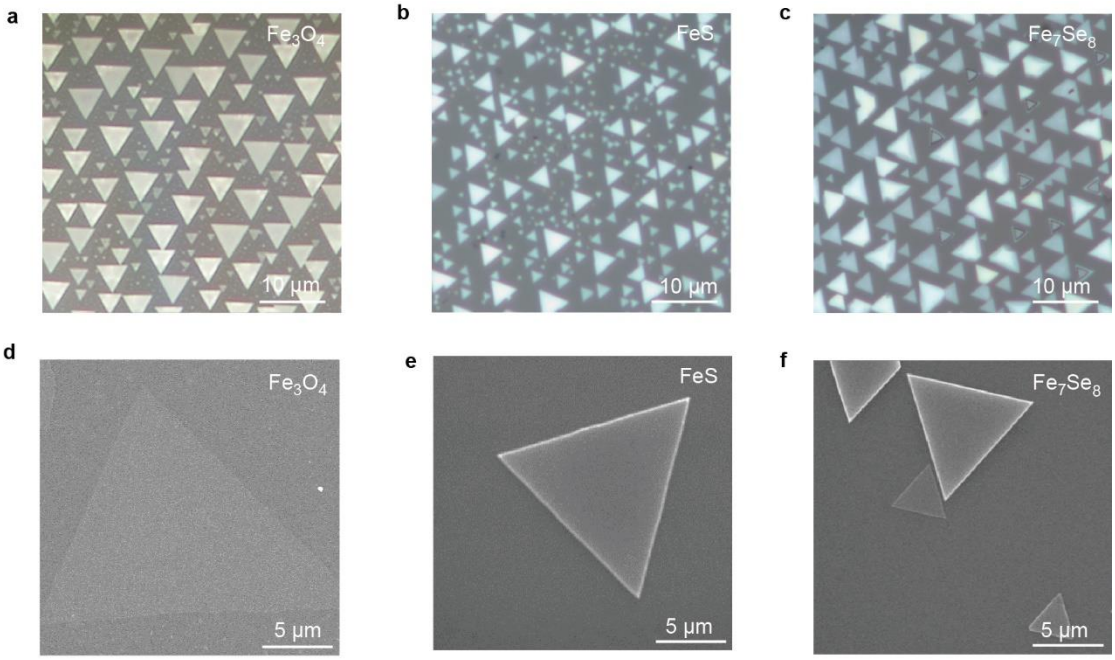

Supplementary Fig. 2 | Morphology of synthesized 2D Fe-based crystals. a-c OM and **d-f** SEM images of Fe_3O_4, FeS, and Fe_7Se_8, respectively.

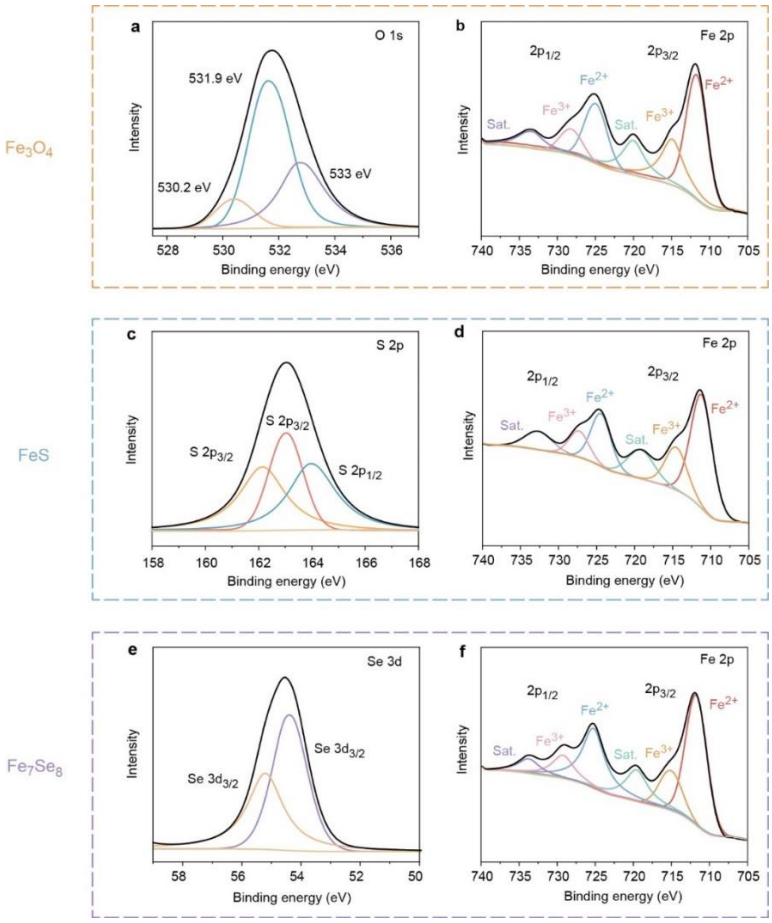

Supplementary Fig. 3 | XPS analysis of 2D Fe-based crystals. a-b Fe 2p and O 1s spectra of Fe_3O_4; **c-d** Fe 2p and S 2p spectra of FeS; **e-f** Fe 2p and Se 3d spectra of Fe_7Se_8.

The bonding states and composition of the 2D Fe-based (Fe_3O_4, FeS, Fe_7Se_8) crystals were further confirmed by X-ray photoelectron spectroscopy (XPS), as shown in Figure S3. The binding energies at ~725.9 and ~712.3 eV correspond to Fe^{3+}, while the peaks at ~722.9 and ~709.8 eV are assigned to Fe^{2+}, consistent with previously reported XPS characteristics of 2D Fe_3O_4, FeS and Fe_7Se_8 crystals. For Fe_3O_4, three distinct peaks located at 530.33, 531.63, and 532.73 eV confirm the presence of O 1s. For FeS, the peaks at 163.95 eV and 162.1 eV in the S 2p orbital are attributed to the S $2p_{1/2}$ and S $2p_{3/2}$ states, respectively. In Fe_7Se_8, the peaks at 54.4 eV and 55.2 eV in the Se 3d orbital correspond to the Se $3d_{5/2}$ and Se $3d_{3/2}$ states, respectively. These XPS results are consistent with previously reported data for Fe_3O_4, FeS, and Fe_7Se_8, confirming the desired chemical composition and typical bonding states of the as-prepared crystals.

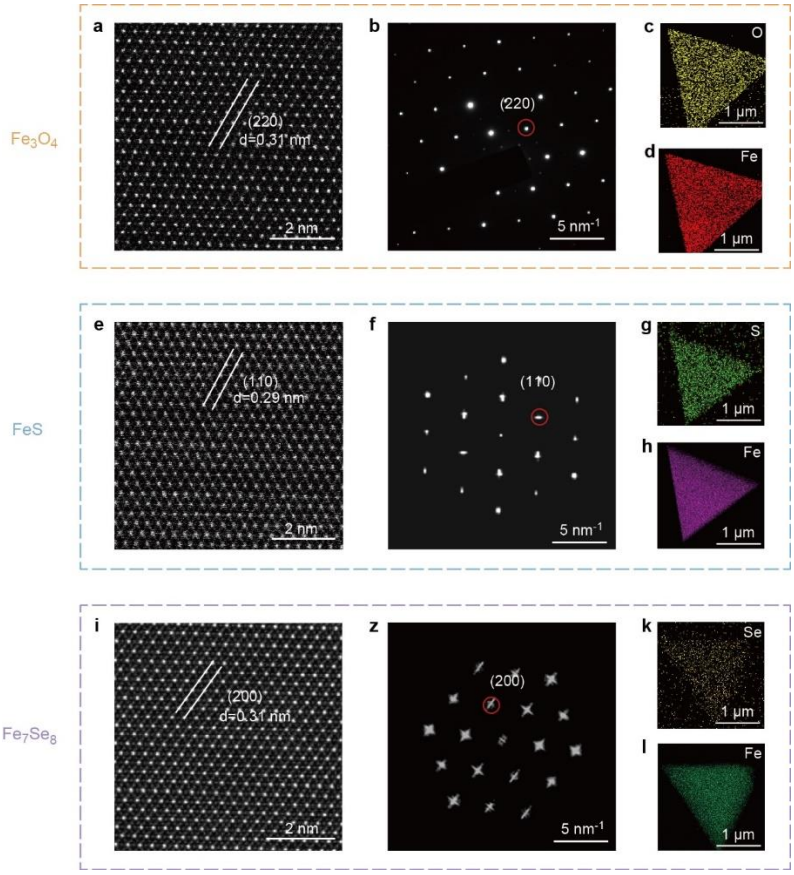

Supplementary Fig. 4 | Composition and structure of 2D Fe-based crystals. a-d HRTEM image, SAED pattern, and TEM-EDS elemental maps of an ultrathin Fe_3O_4 crystals. **e-h** Corresponding characterization of FeS. **i-l** Corresponding characterization of Fe_7Se_8.

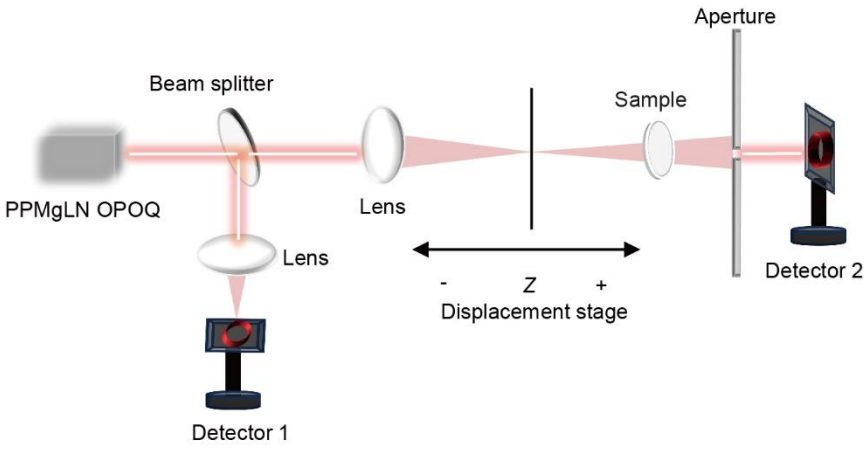

Supplementary Fig. 5 | Schematic of the open-aperture Z-scan setup.

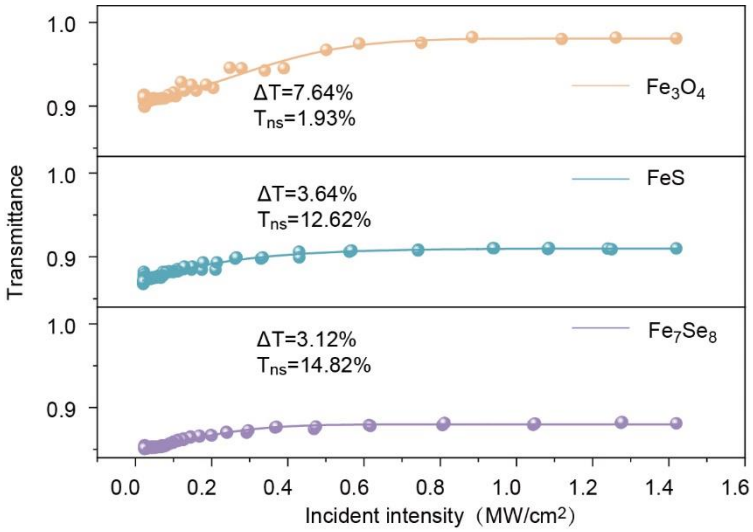

Supplementary Fig. 6 | Normalized transmittance of 2D Fe-based SAs at 2.8 μm.

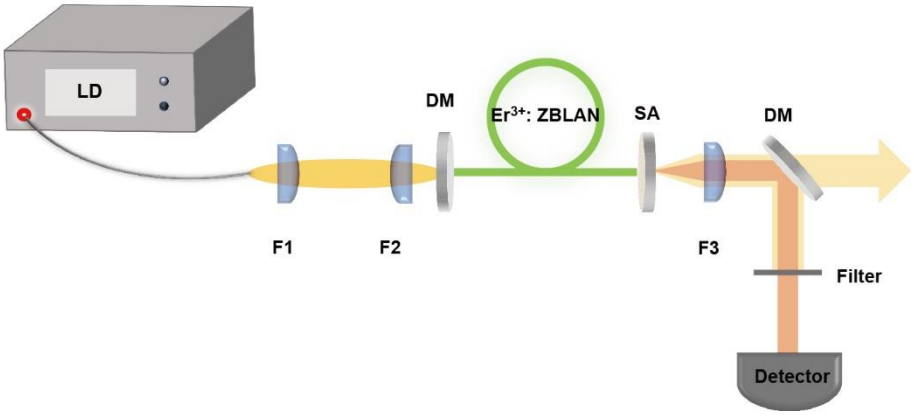

Supplementary Fig. 7 | Schematic of a passively Q-switched Er^{3+}: ZBLAN fiber laser using 2D Fe-based SAs.

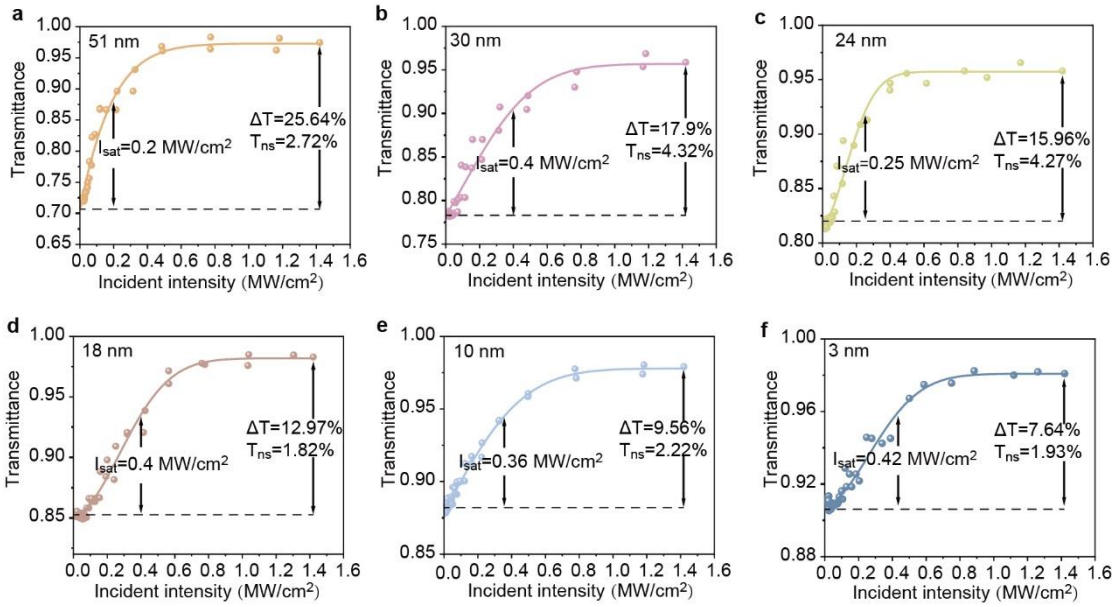

Supplementary Fig. 8 | Nonlinear absorption curves of Fe_3O_4 SA with different thicknesses at 2.8 μm.

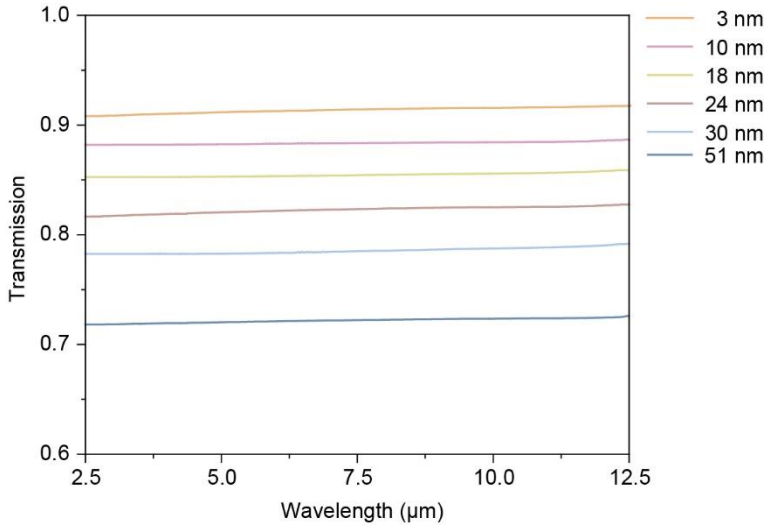

Supplementary Fig. 9 | Mid-infrared transmission spectra of Fe_3O_4 SA with different thicknesses (2.5-12.5 μm).

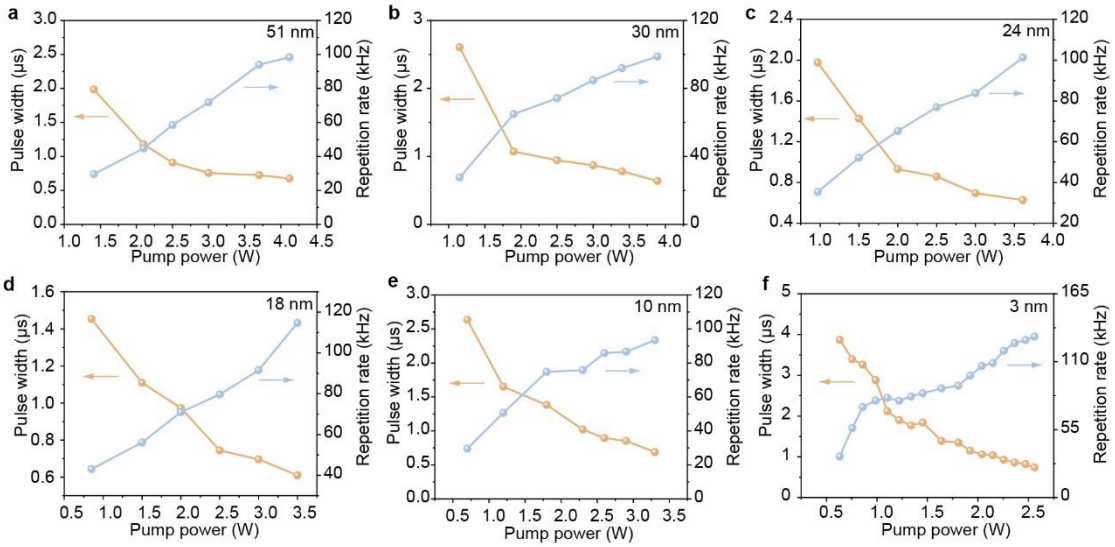

Supplementary Fig. 10 | Thickness-dependent passive Q-switching characteristics (pulse width and repetition rate) of a Fe_3O_4 SA at 2.8 μm.

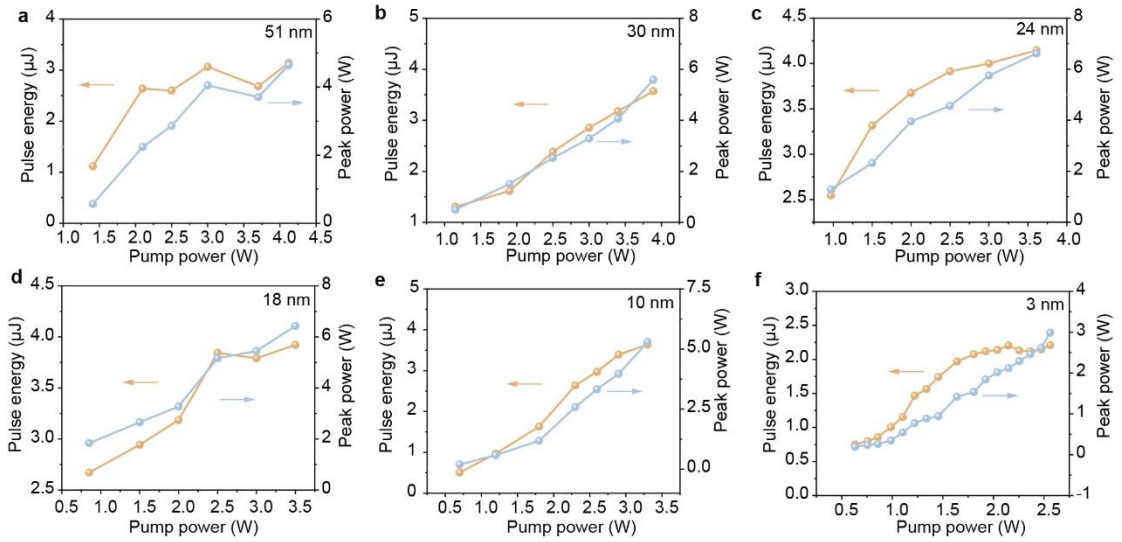

Supplementary Fig. 11 | Thickness-dependent passive Q-switching characteristics (pulse energy and peak power) of a Fe_3O_4 SA at 2.8 μm.

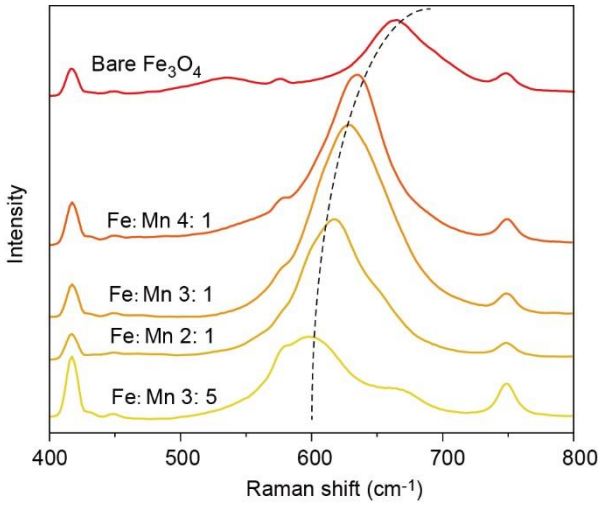

Supplementary Fig. 12 | Redshift of the A_{1g} Raman peak (662 cm^{-1}) of bare Fe_3O_4 as a function of Mn doping concentration.

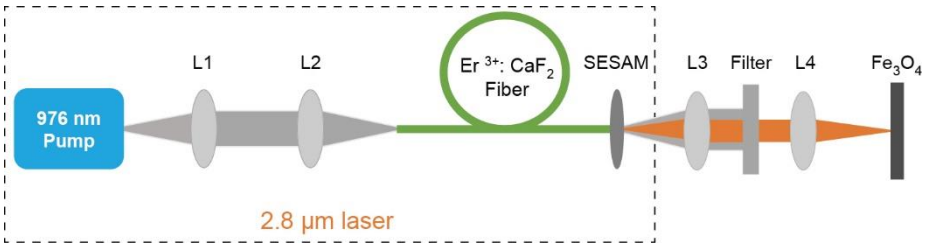

Supplementary Fig. 13 | Schematic of the experimental setup for laser-induced damage threshold test.

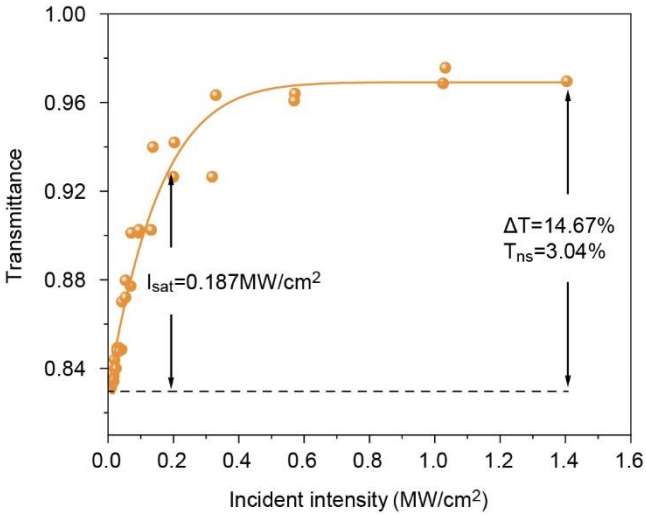

Supplementary Fig. 14 | Nonlinear absorption curves of Mn-Fe_3O_4 at 2.8 μm.